Progress In Electromagnetics Research M, Vol. 116, 177–191, 2023

EMT Image Reconstruction Based on Composite Sensitivity Matrix and Its Application in Defect Detection of Carbon Fiber Wound Hydrogen Tank

Ming Ma[1], Qiong Zhang[2], Ronghua Zhang[3, *], Shiyu Liu[2], Yi Wu[3], and Bailiang Chen[3]

Abstract—Carbon fiber wound hydrogen tanks are widely used in the field of new energy, but their complex multilayer structure makes it difficult to conduct nondestructive testing/structural health monitoring (NDT/SHM). In this paper, electromagnetic tomography (EMT) is used for noncontact in situ defect detection on a carbon fiber wound hydrogen tank. According to its structural characteristics, an open U-shaped sensor array that fits the curvature of the tank body is designed. To improve the quality of reconstructed images, an iterative image reconstruction algorithm based on a composite sensitivity matrix (CSM) is proposed. To verify the performance of the method, the method in this paper is compared with linear back projection (LBP), Landweber iterative algorithm, and the Tikhonov regularization algorithm, and the image quality is evaluated by comparing the image relative error and correlation coefficient. Both simulated and experimental results show that the method proposed in this paper is more accurate in defect localization and higher in quality than traditional image reconstruction algorithms.

1. INTRODUCTION

Hydrogen energy has the advantages of environmental protection, convenient transportation, and low loss, making it an ideal new energy source. At present, a variety of hydrogen storage methods have been developed, among which composite high-pressure tanks are the most widely used and mature hydrogen storage method [1]. Type III composite hydrogen storage tanks usually consist of an innermost aluminum lining and an outer wrapped carbon fiber/epoxy composite layer [2]. This has good strength, stiffness-to-weight ratio, fatigue performance, and corrosion resistance [3]. During transportation and usage, the defects of the tank body not only affect the performance and safety of the hydrogen storage tank but also cause serious safety hazards or even catastrophic accidents.

Hydrogen storage methods can be divided into three types: gas hydrogen storage, liquid hydrogen storage, and solid hydrogen storage. At present, the common hydrogen storage methods are gas hydrogen storage and liquid hydrogen storage. Gaseous hydrogen storage requires compressing the hydrogen in the container to increase the hydrogen storage density and reduce the volume. Liquid hydrogen storage needs to be below 21 K to enable and maintain liquefaction [4]. Ren et al. [5] proposed a comprehensive macro/micro scale (IMM) method to predict the matrix failure of tanks at low temperatures, providing a numerical tool for the reliability analysis of cryogenic composite tanks. Meng [6] et al. proposed an improved progressive damage model and verified the prediction results by using X-ray computed tomography. Various NDT techniques have been used for defect detection of high-pressure gas hydrogen storage tanks, including acoustic emission (AE) [7], digital image correlation (DIC) [8], X-ray [9], ultrasonic guided wave [10], and other methods.

Received 24 February 2023, Accepted 2 May 2023, Scheduled 15 May 2023

* Corresponding author: Ronghua Zhang (rh_zhang_2005@163.com).

[1] School of Life Sciences, Tiangong University, Tianjin 300387, China. [2] School of Control Science and Engineering, Tiangong University, Tianjin 300387, China. [3] School of Artificial Intelligence, Tiangong University, Tianjin 300387, China.

Electromagnetic tomography (EMT) is a real-time nondestructive testing technology based on the principle of electromagnetic induction. It has the advantages of noncontact, fast imaging speed, and no radiation, and has been widely used in biomedicine, rail flaw detection, chemical engineering, and other fields [11, 12]. The damage to the hydrogen storage tank is mainly concentrated in the carbon fiber winding layer and the liner. Although carbon fiber is electrically conductive, it has characteristics of inhomogeneity and anisotropy [13], which make image reconstruction difficult and low in resolution. In the process of image reconstruction, the sensitivity matrix is an important factor affecting the quality of image reconstruction. Ye et al. [14] proposed an image reconstruction based on an extended sensitivity matrix, which improved the image quality and stability compared with the conventional Landweber iterative algorithm. Zhang et al. [15] proposed a differential sensitivity matrix constructed based on the reference and measured fields. This can suppress the adverse effects of soft-field effects on image reconstruction. Zhang and Yin [16] proposed a new method for determining the weighting factors of parallel model (PM) and series model (SM) sensitivity matrices, forming a mixed normalization model sensitivity matrix to improve the accuracy and shape fidelity of reconstructed images. Tang et al. [17] pointed out that the electrical capacitance tomography (ECT) sensitivity coefficient can be expressed as the superposition of two components, and by considering the distribution of charge and dielectric constant at the same time, the influence of dielectric charging on image reconstruction can be suppressed.

EMT is sensitive to both conductivity and permeability, and traditional methods only focus on one parameter to image it. In this paper, two methods of sensitivity matrix combination are proposed. Through the analysis of composite sensitivity matrix coefficients, the structural defects of multi-layer and different materials can be detected.

Due to the multilayer heterostructure of the carbon fiber-wound hydrogen tanks, the different materials that it contains have varying sensitivities to different physical quantities. In this paper, a composite sensitivity matrix of the electric and magnetic field strengths is used to improve the detection accuracy of the EMT detection system for defects in different depths of carbon fiber wound hydrogen tanks.

2. APPLICATION OF ELECTROMAGNETIC TOMOGRAPHY DETECTION

2.1. Sensor Optimization

Electromagnetic tomography (EMT) systems are used to visualize the spatial distribution of magnetic permeability and conductivity within a region [18]. The sensor array of most EMT systems consists of several coils that are distributed around the imaging region [19], as shown in Figure 1. The excitation coil generates an AC magnetic field in the measured area, and the induced voltage of the pick-up coil changes due to the variation in the local electrical parameters (permeability and conductivity) of the detected specimens [20]. To fit the detection object in this paper and facilitate hand-held scanning, a open sensor structure was designed. The sensor coil array consists of eight coils arranged side by side in a U shape.

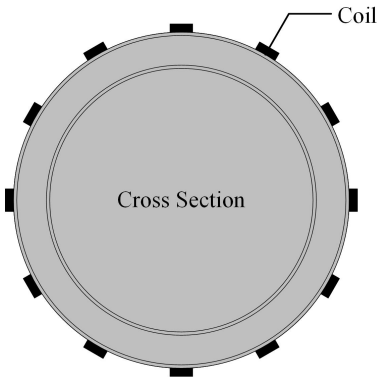

Figure 1. Typical EMT sensors.

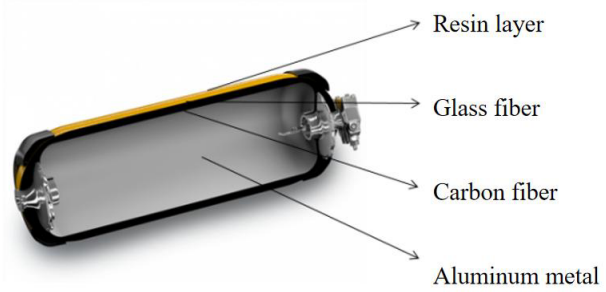

Figure 2. Structure diagram of hydrogen storage tank.

The hydrogen storage tank has a four-layer structure, as shown in Figure 2, with aluminum metal, carbon fiber, glass fiber, and resin layers. Since damage to the fiber layer and aluminum metal layer of the hydrogen storage tank reduces the bearing capacity of the container [3], only the fiber layer and aluminum metal layer are discussed in this paper.

A finite element model (FEM) of a three-layer ring structure is established using COMSOL Multiphysics software. The material property of the aluminum metal layer is set to 2 mm thick, and the layer is used to simulate the innermost metal liner of the hydrogen storage tank. The outer two-layer structure simulates the radially wound and hoop wound structures of carbon fibers by setting the values of electrical conductivity in different directions; both are 3 mm thick. In this paper, an open sensor with a U-shaped structure sensor array is designed and composed of 8 coils. The 8 coils fit the tank body and are distributed in a row; 8 coils are cyclically excited and pick up induction signals. When the red coil (Figure 3) is selected as the transmitting coil, the remaining 7 coils act as the receivers. The 8 coils are excited and pick up signals in turn, and a total of 56 ($8 \times 7 = 56$) induced voltages are obtained as a set of measurement data, as shown in Figure 3.

Table 1 lists the geometric and material description of the hydrogen storage tank. Depending on the overall dimensions of the tank, the sensor is designed. The parameters of the designed sensor are as follows: the inner radius of the coil used in this paper is 3 mm; the outer radius is 4 mm; and the

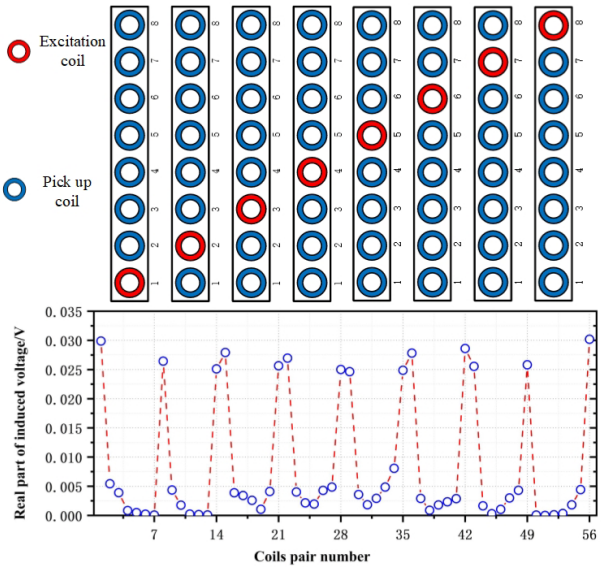

Figure 3. A set of data.

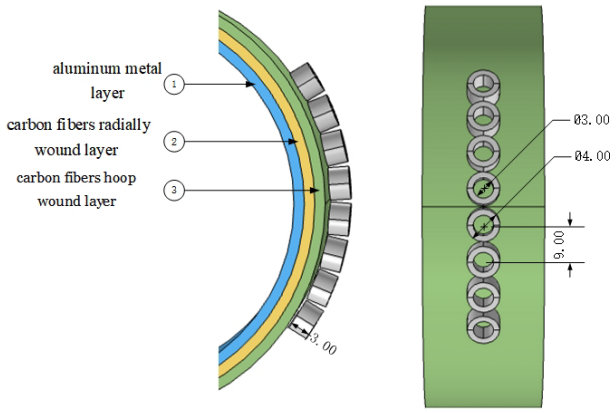

Figure 4. Simulation model.

Table 1. Description of hydrogen storage tank geometry and material.

Type	Outer Diameter (mm)	Water Volume (L)	Length (mm)	Weight (kg)
CRPIII-145-6.8-30-T	157	6.8	528	4.1
Materials consist of	Aluminum inner shell, fully wrapped with high strength carbon fiber, glass fiber and epoxy resin.			
Technical standard	EN, DOT, ISO upon customers' demand			
Service pressure	30 Mpa			
Working Pressure	4500 psi			
Inspection cycle	3 years			
Lifespan of product	15 years			
Inlet thread	M18 × 1.5 mm			

height is 3 mm. The center-to-center spacing of the coils is 9 mm. To make the sensor fit the tank's body, the radius from the center of the coil to the center of the tank is chosen to be 160 mm, and the overall length of the sensor is 67 mm. The front and side views of the simulation model are shown in Figure 4.

2.2. EMT Equipment

A diagram of the EMT equipment is shown in Figure 5(a) and is composed of three parts: sensor, data acquisition and processing, and image reconstruction. It is implemented by Xilinx's ZYNQ series model XCZ7020-CLG484 FPGA, which integrates the ARM Cortex-A9 processor system (PS) and the programmable logic part (PL) of the FPGA. Compared with traditional embedded CPUs, ZYNQ has a powerful parallel processing capability. The excitation signal is generated by the direct digital synthesis (DDS) signal inside the FPGA, and the excitation signal is distributed to the coil by the analog switch. The digital signal is converted into an analog signal by a D/A converter and then output through an amplifier. When passing through the defect site and compared with the excitation signal, the amplitude and phase of the received signal change, and the A/D conversion converts the analog signal into a digital signal that is controlled and collected by the FPGA. Finally, signal demodulation is implemented by the FPGA, and the relevant information reflecting the change in the target field is extracted and then transmitted to the host computer through Ethernet to reconstruct the image.

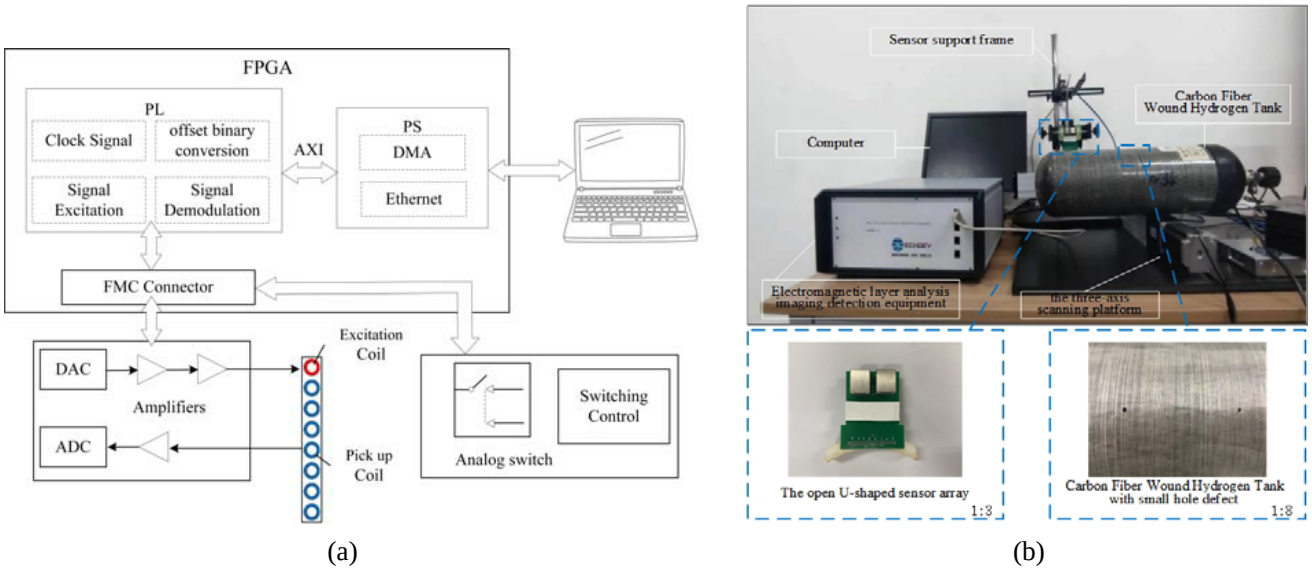

Figure 5. EMT equipment. (a) Diagram. (b) Application.

The discrete version of the pick up coil signal is

$$S_r(n) = A_r \sin\left(\frac{2\pi f_r n}{f_s} + \theta\right), \quad 0 \le n \le N-1 \tag{1}$$

where A_r, θ, f_s, and N are the amplitude, phase, sampling frequency, and sampling number of the collected signal, respectively.

The picked up signal is multiplied by the reference cosine and sine, and then a low-pass filter ($F[n]$) is used to demodulate [21]:

$$Y_1[n] = S_r(n) \cdot \sin\left(\frac{2\pi f_r n}{f_s}\right) \bigotimes F[n] \approx \frac{1}{2} A_r \cos\theta \tag{2}$$

$$Y_2[n] = S_r(n) \cdot \cos\left(\frac{2\pi f_r n}{f_s}\right) \bigotimes F[n] \approx \frac{1}{2} A_r \sin\theta \tag{3}$$

The application of the equipment is shown in Figure 5(b). The programmable three-axis scanning platform has been used to scan the tank and has been loaded with sensors. The scan area is a square. During the scan, 16 sampling points have been measured. The sampling frequency is 100 kHz. The 16 sets of collected data are then transmitted to the computer to obtain images with defect information, which are used to reconstruct the image.

3. IMAGE RECONSTRUCTION ALGORITHM

3.1. Calculation of the Sensitivity Matrix

As the prior information of image reconstruction, the sensitivity matrix is a measure of the magnitude of change of the induced voltage to a variation of the electromagnetic parameters of the materials in the imaging region. According to the EMT principle, when the conductivity, magnetic permeability, and permittivity of the medium in the measured object field region change, the change of F of the measured value is expressed as [22].

$$\delta F = \int_V \left(S_\sigma \delta\sigma + S_\mu \delta\mu + S_\varepsilon \delta\varepsilon\right) d\mathbf{V} \tag{4}$$

where F is a function of the electric and magnetic fields at a point, S_σ the sensitivity of the conductivity, S_μ the sensitivity of the magnetic permeability, and S_ε the sensitivity of the permittivity of the medium.

The voltage of the pickup coil in the EMT system is expressed as

$$V_R = \int_V f(\mathbf{E}, \mathbf{H}) dV = \int_V \mathbf{E}_T \cdot \frac{\mathbf{J}_R}{I_R} dV \tag{5}$$

where V_R is the induced voltage, $\mathbf{E}_T$ the electric field generated by the excitation coil, $\mathbf{J}_R$ the current in pick up coil, I_R the modulus of the current vector, and $\frac{\mathbf{J}_R}{I_R}$ the unit vector in the direction of the receiver coil axis.

Maxwell's equations when being excited by a sinusoidal signal are expressed as

$$\begin{cases} \nabla \times \mathbf{E} = -\dfrac{\partial \mathbf{B}}{\partial t} = -j\omega\mu\mathbf{H} \\ \nabla \times \mathbf{H} = \mathbf{J} + \dfrac{\partial \mathbf{D}}{\partial t} = \mathbf{J}_{EX} + (\sigma + j\omega\varepsilon)\mathbf{E} \end{cases} \tag{6}$$

where $\mathbf{J}_{EX}$ is the externally applied current density.

Defining a Poynting vector $S_{AB} = \mathbf{E}_A \times \mathbf{H}_B$, the volume integral of its divergence is:

$$\int_V \left(\mathbf{H}_B \cdot \nabla \times \mathbf{E}_A - \mathbf{E}_A \cdot \nabla \times \mathbf{H}_B\right) dV = \oint_S \left(\mathbf{E}_A \times \mathbf{H}_B\right) \cdot \mathbf{n} dS \tag{7}$$

A is used as a transmitting coil, and B is used as a pickup coil. Substituting (6) into (7) and then (7) into (5), then calculating the finite differential of (5) and neglecting higher order terms, we have

$$\begin{aligned} \int_V \left(\delta\mathbf{E}_A \cdot \mathbf{J}_{EXB}\right) dV \;=\; & \int_V \left(\mathbf{E}_A \cdot \mathbf{E}_B \delta\sigma + j\omega \mathbf{E}_A \cdot \mathbf{E}_B \delta\varepsilon - j\omega \mathbf{H}_A \cdot \mathbf{H}_B \delta\mu\right) dV \\ & + \oint_S \left(\mathbf{E}_B \times \delta\mathbf{H}_A - \delta\mathbf{E}_A \times \delta\mathbf{H}_B\right) \cdot \mathbf{n} dS \end{aligned} \tag{8}$$

Comparing (4) and (8) and assuming that the boundary is sufficiently far away to completely enclose the fields, the surface integral in (8) vanishes, and the mathematical expression of sensitivity can be obtained:

$$\begin{cases} S_\sigma = \mathbf{E}_A \cdot \mathbf{E}_B \\ S_\mu = -j\omega \mathbf{H}_A \cdot \mathbf{H}_B \end{cases} \tag{9}$$

where $\mathbf{E}_A$ and $\mathbf{E}_B$ are the electric field strengths when the excitation coil and the pick up coil are excited. $\mathbf{H}_A$ and $\mathbf{H}_B$ are the magnetic field strengths when the excitation coil and pick up coil are excited. Electromagnetic detection is not sensitive to the dielectric constant, and our study is only

focused on materials that are electrically or magnetically conductive. Therefore, there has been no specific study conducted on the sensitivity matrix of the dielectric constant.

According to the definition of the vector magnetic potential $A : B = \nabla \times \mathbf{A}$ and $\nabla \times \mathbf{E} = -\frac{\partial \mathbf{B}}{\partial t} = -j\omega\mathbf{B}$, one obtains:

$$\mathbf{E} = -j\omega\mathbf{A} \tag{10}$$

Therefore, the conductivity sensitivity can be expressed as:

$$S_\sigma = \mathbf{E}_A \cdot \mathbf{E}_B = -\omega^2 \mathbf{A}_A \cdot \mathbf{A}_B \tag{11}$$

where ω is the operating frequency of the system, and $\mathbf{A}_A$ and $\mathbf{A}_B$ are the vector magnetic potential distributions of the excitation coil and receiving coil when they are excited by unit current, respectively.

The imaging effects of two sensitivity matrices of two coils are calculated by the field quantity extraction method of (9) and (11). The imaging results of the conductivity and the permeability sensitivity matrix are shown in Figure 6. The area around the coil of the conductivity sensitivity matrix of the sensor array is highly sensitive, and the permeability sensitivity matrix is more sensitive to the area directly below the coil. The sensitivity of the distribution does not fully reflect the defect information, and there are peak areas. This affects the accuracy of image reconstruction.

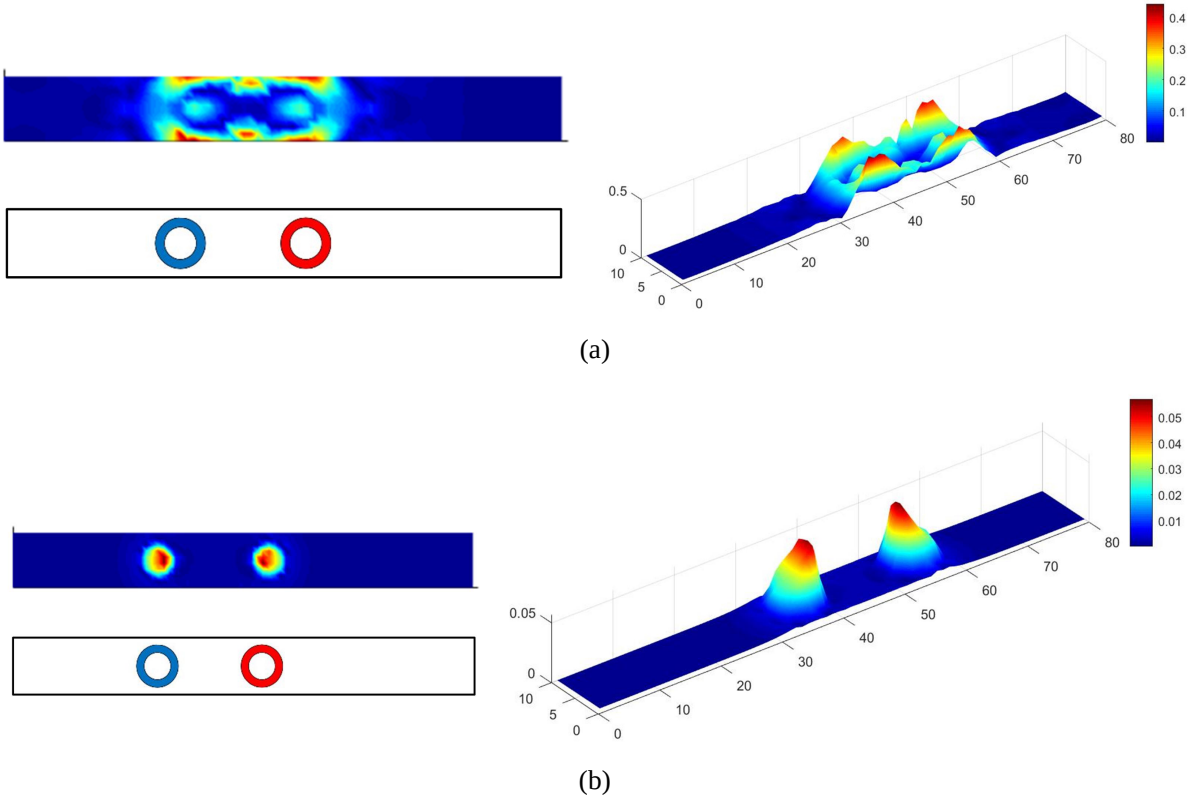

Figure 6. Imaging result of dual-coil model. (a) Conductivity sensitivity matrix. (b) Permeability sensitivity matrix.

In view of the above problems, this paper combines the permeability sensitivity matrix with the conductivity sensitivity matrix under the same image reconstruction algorithm. The composite sensitivity matrix can be expressed as

$$S_O = (p_\sigma S_\sigma + p_\mu S_\mu) \tag{12}$$

where p_σ and p_μ are the weighting factors of the conductivity sensitivity and permeability sensitivity, respectively, optimized according to the analysis of imaging results. S_σ and S_μ are the normalized results of the conductivity sensitivity and permeability sensitivity, respectively, and S_O is the optimized sensitivity matrix.

Mean filtering has been used on the sensitivity matrix, as described in (13), to obtain better reconstructed image results. The principle of mean filtering is to select a template containing N pixels, where e is the pixel in the center of the template. The average value of all pixels is calculated, covered by the template as the center pixel of the module.

$$S_{1(i,j)}(e) = \frac{1}{N}\sum_{k=1}^{N} S_{O(i,j)}(k) \tag{13}$$

where i and j are the rows and columns of pixels, respectively, and k is the number of surrounding pixels.

Structural similarity (SSIM) is commonly used to measure the similarity of digital images [23]. It has also been applied to evaluate the similarity of reconstructed images [24]. Therefore, in order to select appropriate weighting factors, this paper introduces SSIM to measure the similarity of reconstructed images when different weighting factors are selected.

$$\mathrm{SSIM}_{(s,\hat{s})} = \frac{(2\mu_s\mu_{\hat{s}} + C_1)(2\sigma_{s\hat{s}} + C_2)}{(\mu_s{}^2 + \mu_{\hat{s}}{}^2 + C_1)(\sigma_s{}^2 + \sigma_{\hat{s}}{}^2 + C_2)} \tag{14}$$

where $\hat{s}$ and s are the reconstructed image and real conductivity image; μ_s and $\mu_{\hat{s}}$ are the mean values of the real and reconstructed conductivity images; σ_s and $\sigma_{\hat{s}}$ are the standard deviations of the real and reconstructed image conductivities; $\sigma_{s\hat{s}}$ is the covariance of the real and reconstructed image conductivities; and C_1 and C_2 are constants used to prevent division by zero.

The range of SSIM is -1 to 1. The abscissa in Figure 7(a) is the ratio of p_σ to p_μ. It can be seen from the figure that when the ratio is 3/2, that is, p_e is 0.6, and p_h is 0.4, the result of SSIM is the largest, indicating that the reconstructed image is highly similar to the real image when these two values are used as weight factors. When calculating SSIM vs p_σ/p_μ in Figure 7, s and $\hat{s}$ use the real image and image estimate of the defect as shown in Figure 7(b), where the size of the defect is 1 mm. Changing the size of the defect gives similar results.

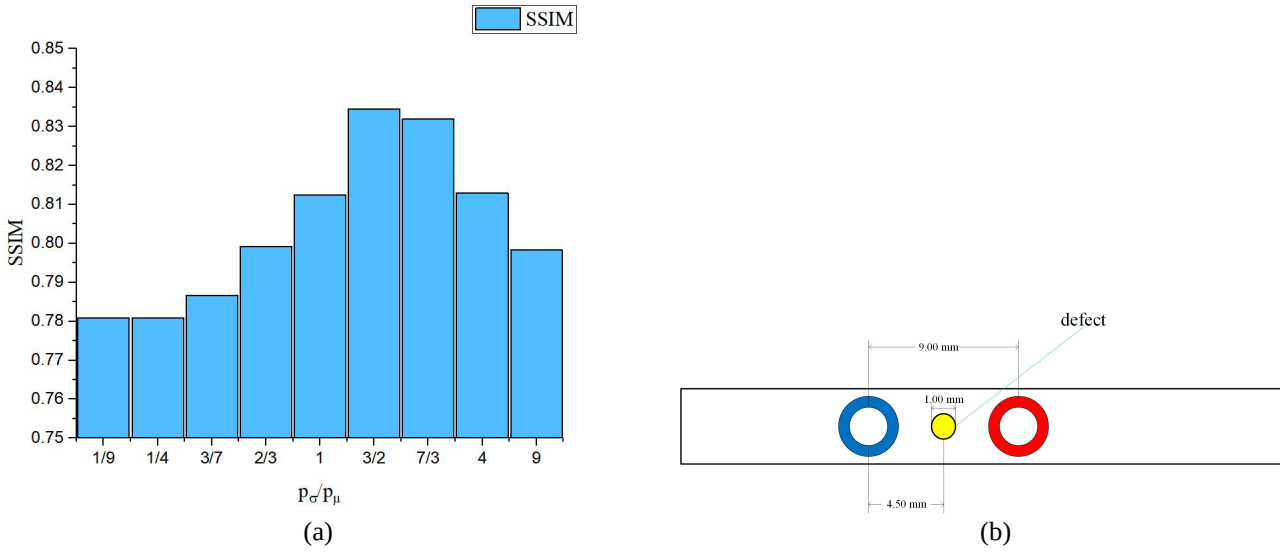

Figure 7. SSIM values for different weighting factors and schematic diagram of the model with defects. (a) SSIM values. (b) The model with defects.

3.2. Landweber Iterative Method of Composite Sensitivity Matrix (CSM)

Common image reconstruction algorithms include Linear Back Projection (LBP), Tikhonov regularization, and Landweber iteration method. The first two algorithms are represented by (15)

and (16). The computation time is short, but the obtained image error is large, which is suitable for scenes that attach importance to the speed of image generation.

$$g = S^T U \tag{15}$$

$$g = \left(S^T S + \mu I\right)^{-1} S^T U \tag{16}$$

where U is the column vector of the measured voltage, S the sensitivity matrix, μ the regularization parameter, I the identity matrix, and g the conductivity distribution on each mesh [25].

Landweber iteration method is an iterative imaging algorithm [26]. Due to its iterative method, the calculation time is long, but the error of the reconstructed image obtained is small, which can improve the defect location and defect type discrimination. Thus we have chosen the Landweber method and have modified it to improve performance. Its iterative form is expressed as

$$\begin{cases} g_0 = 0 \\ g_{k+1} = g_k + \beta S^T \left(U - S g_k\right) \end{cases} \tag{17}$$

where g_0 is the initial value of the iteration, β the gain factor, g_k the image gray scale value of the kth iteration, S the sensitivity matrix, and U the measured voltage vector.

The gain factor β in this paper is taken as $2/(\lambda_{\max} + \lambda_{\min})$, where $\lambda_{\max}$ and $\lambda_{\min}$ are the largest and smallest eigenvalues of the $(p_\sigma S_\sigma + p_\mu S_\mu)^T (p_\sigma S_\sigma + p_\mu S_\mu)$ matrix, respectively. The iterative form of the improved Landweber algorithm is

$$\begin{cases} g_0 = 0 \\ g_{k+1} = g_k + \dfrac{2\beta {S_1}^T \left(U - S_1 g_k\right)}{\lambda_{\max} + \lambda_{\min}} \end{cases} \tag{18}$$

Figure 8 shows the imaging results of the sensitivity matrix of the dual-coil model using the above method.

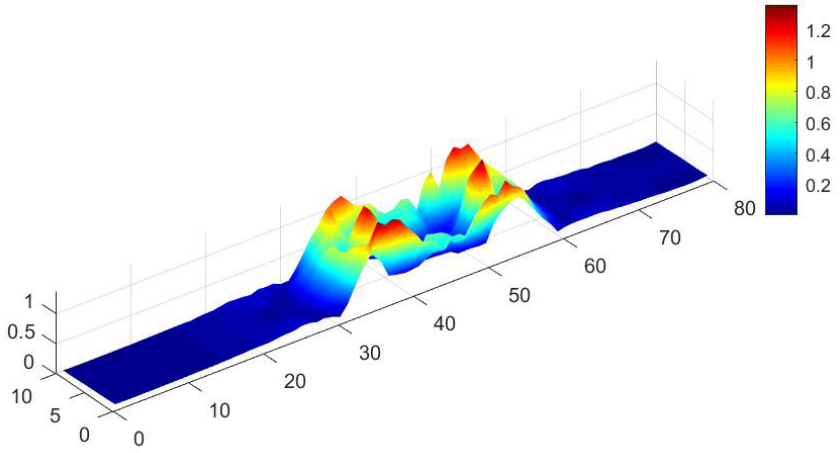

Figure 8. Imaging result of composite sensitivity matrix of dual-coil model.

4. SIMULATION AND EXPERIMENTAL IMAGE RECONSTRUCTION

4.1. Simulation Verification

Hydrogen storage tanks are prone to structural defects under the action of high-cycle fatigue loads and physical shocks. Among them, the fiber fracture defect of the carbon fiber wound layer and the metal structural defect of the inner aluminum layer have a significant impact on the overall mechanical

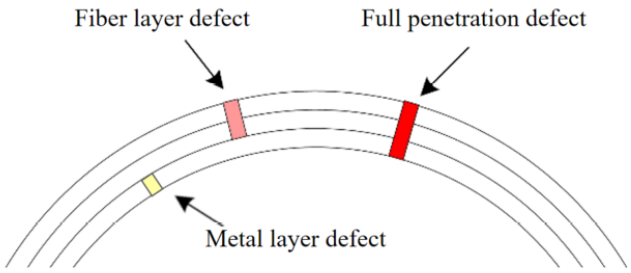

Figure 9. Three defects of simulation design.

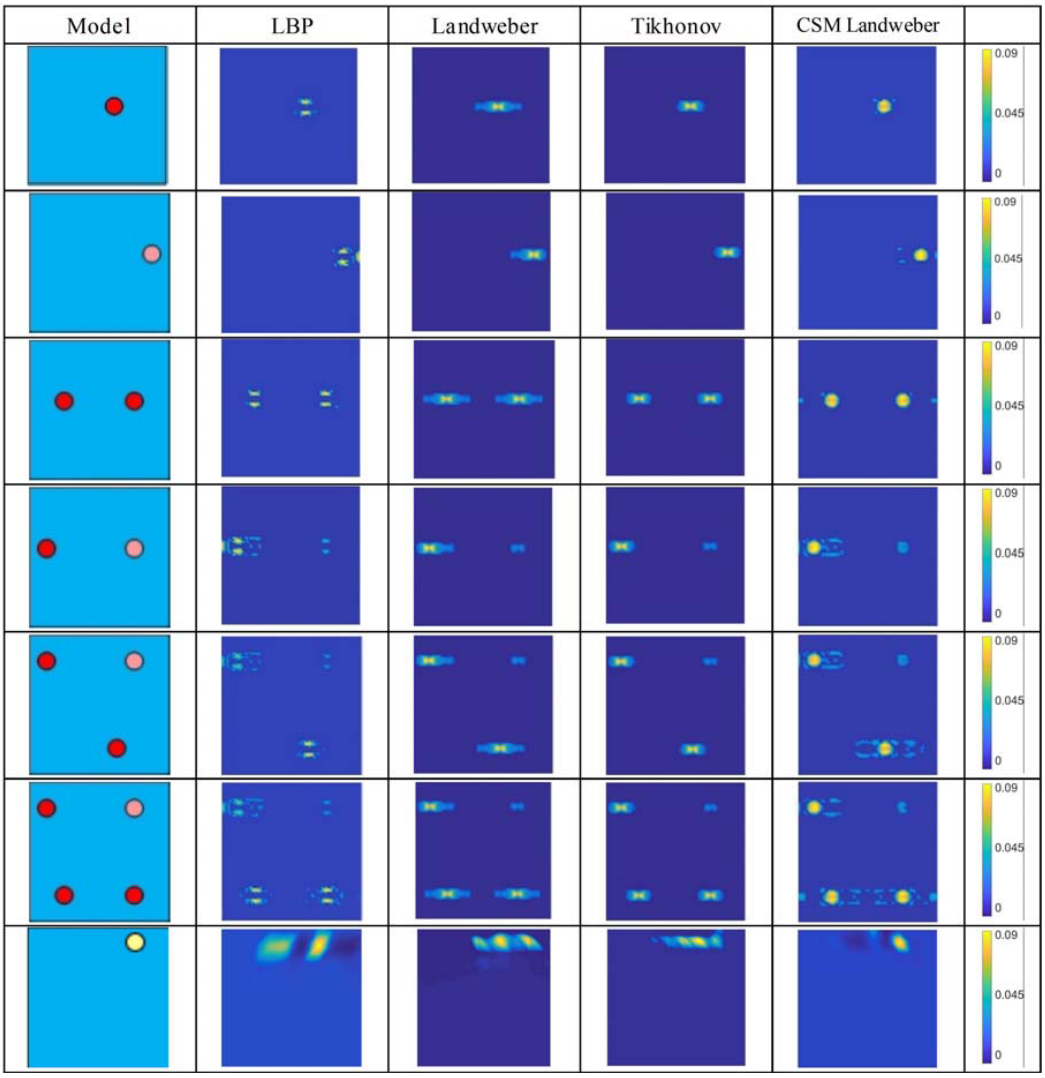

Figure 10. Reconstruction result of simulated image.

properties of the tank. In this paper, three types of defects are selected, which are full penetration defects, fiber layer defects, and metal layer defects, as shown in Figure 9 [26].

First, the surface of the hydrogen storage tank model in the electromagnetic field simulation software is meshed. In this paper, the rectangular detection area is meshed into 800 elements; excitation

signals are applied to 8 coils; and the electromagnetic parameters of each meshed element under the excitation of a single coil are calculated. In order to compare the reconstruction effects of different algorithms, seven defect distributions, as shown in the first column of Figure 10, are designed for simulation experiments. The collected data are imaged using different imaging algorithms: LBP, Tikhonov, Landweber, and the algorithm presented in this paper (improved Landweber, denoted CSM Landweber in what follows). The results are shown in Figure 10.

From the analysis of the simulation results, for different object field distributions, the LBP algorithm has the worst performance. The detection results of the Tikhonov and Landweber algorithms are basically the same. The difference is that the Landweber algorithm has more artifacts. Compared with other algorithms, the proposed algorithm can better reflect the shape characteristics of the defect, and there are fewer artifacts. To further analyze the quality of the reconstructed images, the relative error (RE) and correlation coefficient (CC) are introduced. The four image reconstruction algorithms are used to analyze the imaging results of different defect types. RE and CC are defined as follows:

$$\mathrm{CC} = \frac{\sum_{i=1}^{N} (\sigma_i - \bar{\sigma})(\sigma_i^* - \bar{\sigma}^*)}{\sqrt{\sum_{i=1}^{N} (\sigma_i - \bar{\sigma})^2 \sum_{i=1}^{N} (\sigma_i^* - \bar{\sigma}^*)^2}} \tag{19}$$

$$\mathrm{RE} = \frac{\|\sigma - \sigma^*\|_2^2}{\|\sigma^*\|_2^2} \tag{20}$$

where N is the number of cells in the reconstructed image, σ the conductivity or permeability distribution of the reconstructed image, and $\sigma*$ the actual conductivity or permeability distribution of the original image. $\bar{\sigma}$ and $\bar{\sigma}^*$ represent the average of σ and σ^*, respectively. According to the imaging results of the different algorithms of six different models shown in Figure 10, the correlation

Table 2. Comparison of correlation coefficients of different image reconstruction algorithms.

Model	LBP	Landweber	Tikhonov	CSM Landweber
1	0.0881	0.6107	0.6275	0.6577
2	0.1095	0.6561	0.6668	0.6709
3	0.1318	0.6403	0.6630	0.6878
4	0.2055	0.5632	0.5654	0.5766
5	0.1477	0.5756	0.5954	0.6174
6	0.1912	0.5974	0.6132	0.6328
7	0.1107	0.5298	0.5432	0.6638

Table 3. Comparison of relative error of different image reconstruction algorithms.

Model	LBP	Landweber	Tikhonov	CSM Landweber
1	1.429	1.2236	1.0623	0.9473
2	1.6871	1.149	0.9879	0.9347
3	1.4339	1.2478	1.0209	0.9137
4	1.425	1.0824	0.9566	0.9183
5	1.429	1.2382	1.0063	0.9327
6	1.4425	1.2097	0.9884	0.9153
7	1.5936	1.3096	1.3164	0.9217

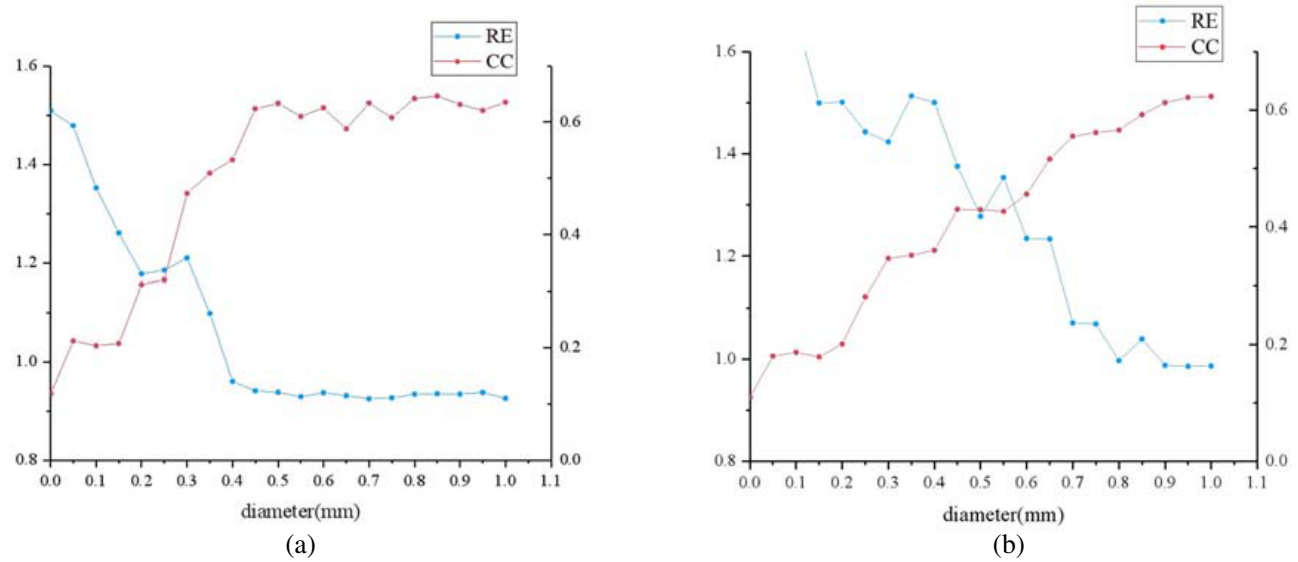

Figure 11. Relative error (RE) and correlation coefficient (CC) results of composite sensitivity matrix imaging results with different defect diameters. (a) External defect. (b) Internal defect.

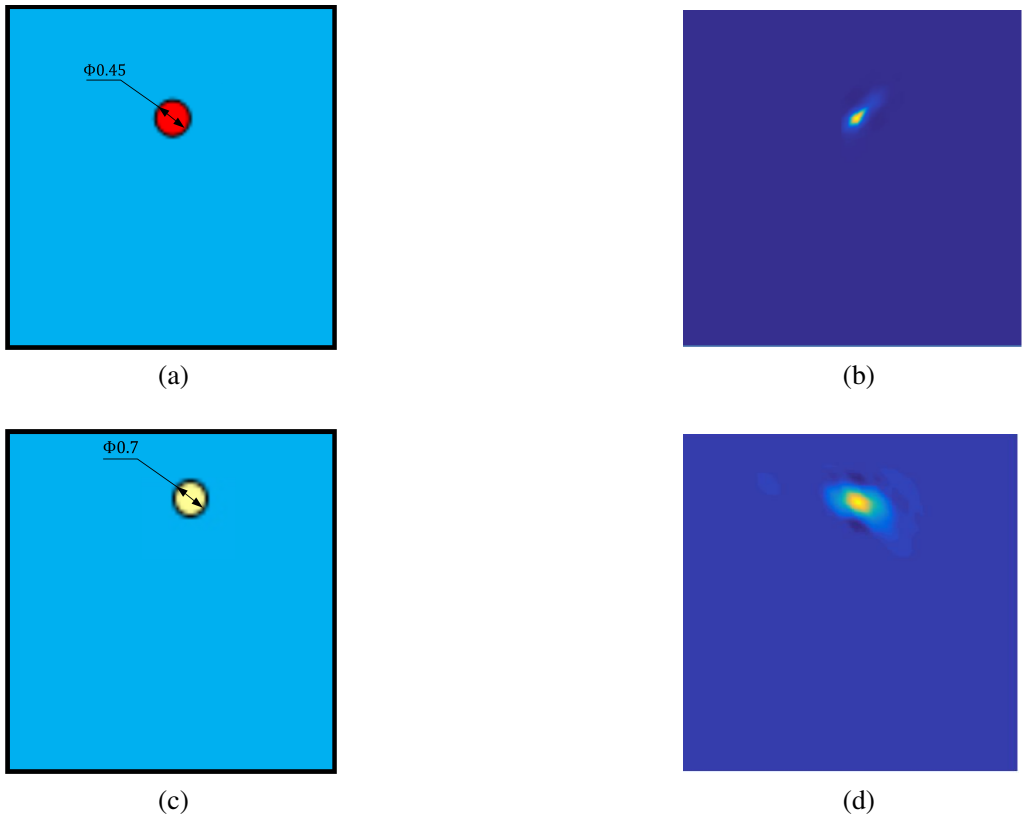

Figure 12. Minimum detection size of image reconstruction. (a) External defect model. (b) Minimum detection size of external defect. (c) Internal defect model. (d) Minimum detection size of internal defect.

coefficient and relative error of the reconstructed image are calculated, and the results are shown in Table 2 and Table 3.

Tables 2 and 3 show that for the object field distribution shown in Figure 10, the relative errors of the algorithms given in this paper are smaller than those of the other algorithms, and the correlation coefficients are larger than those of other algorithms for the same defect model. That is, the image reconstructed by the proposed algorithm has the best fit with the original image and can reflect the defect information more accurately.

In order to discuss the minimum defect size that can be detected by the method proposed in this

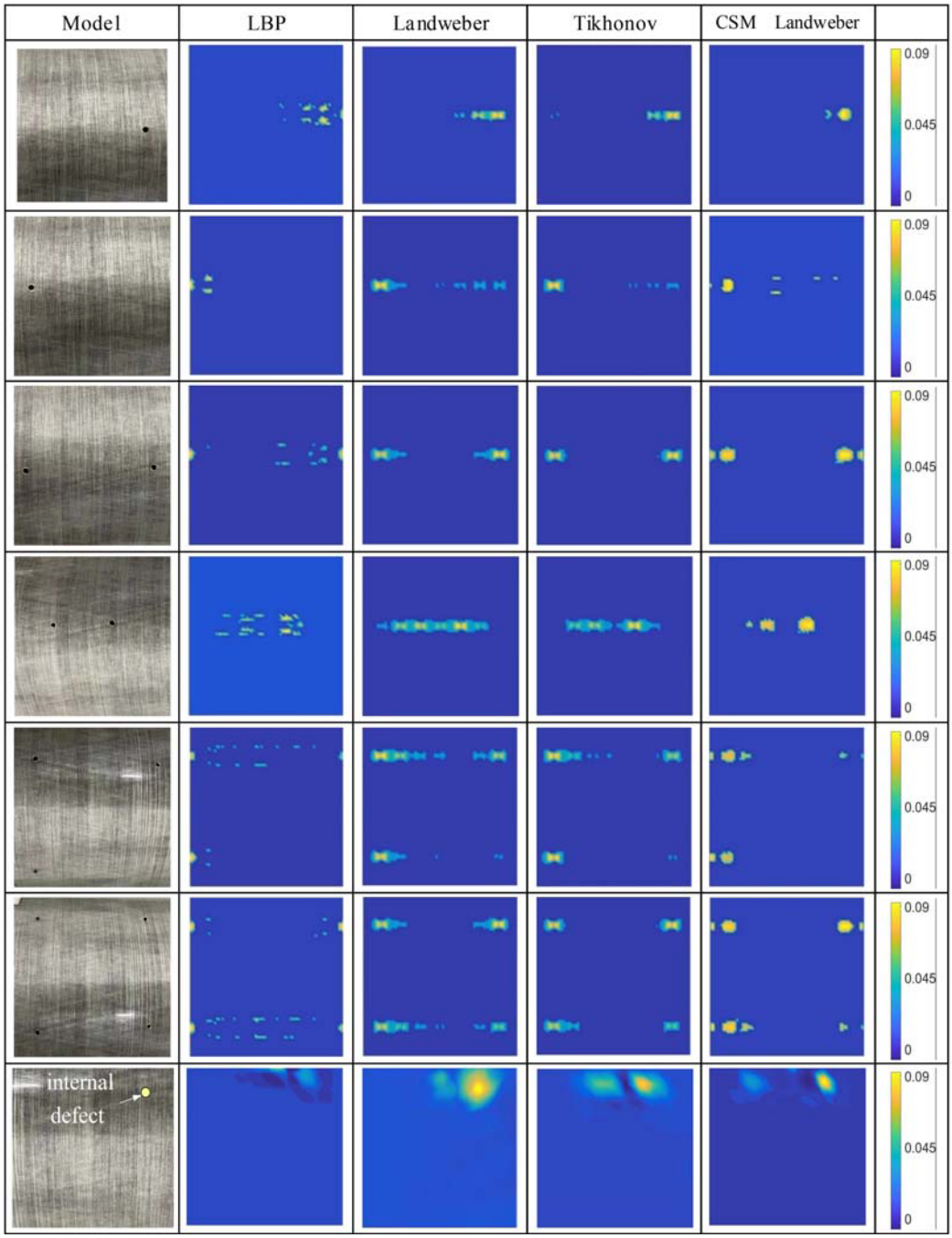

Figure 13. Reconstruction results of experimental images.

paper, RE and CC values of the reconstructed image are calculated respectively by changing the size of defect diameter in simulation, as shown in the curve in Figure 11. CC increases with the increase of defect diameter, while the value of RE is opposite. When the diameter of external defect (a) is greater than 0.4 mm, and the diameter of internal defect (b) is greater than 0.7 mm, the two image evaluation indexes are stable.

As shown in Figure 12, the tank exhibits external defects with a diameter of 0.45 mm and internal defects with a diameter of 0.7 mm, which is the minimum defect size that can be detected by the method proposed in this paper. Smaller-sized defect reconstruction cannot yield satisfactory results with the proposed algorithm.

4.2. Experimental Image Reconstruction

To further verify the effectiveness and feasibility of the proposed method, a defect detection test was carried out on the actual model using the structure shown in Figure 5. In this paper, only the results of the assay at room temperature are discussed. According to the simulation design defect distribution, different types of round-hole defects with a radius of 1 mm are manufactured. Models 1–6 are external defects of the bottle body, and model 7 is an internal defect with a diameter of 1.5 mm. The defect positions of model 7 have been marked with a yellow circle (Figure 13). The experimental reconstruction results of each damage distribution are shown in Figure 13.

Both the Tikhonov regularization algorithm and Landweber iteration method can accurately locate the defects on the hydrogen storage tank, but there are many artifacts, and these methods cannot reflect the shape characteristics of the defects. In the actual measurement, the algorithm proposed in this paper is consistent with the results obtained in the simulation. Compared with other algorithms, the proposed method reduces artifacts and improves accuracy.

5. CONCLUSION

Based on electromagnetic tomography technology, a detection method for hydrogen storage tank defects was proposed. An 8-coil U-shaped sensor array has been designed for defect detection of carbon fiber-wound hydrogen tanks, and the sensitivity matrix was calculated in the simulation model. To improve the quality of the reconstructed image, the Landweber iteration method has been optimized, and a CSM Landweber iteration method that combines permeability and conductivity has been proposed. According to the simulation results, the relative error (RE) and correlation coefficient (CC) for the proposed method, as well as the LBP, Landweber, and Tikhonov methods, have been calculated. Through comparison and analysis, the reliability of the method has been proven. The experimental results at room temperature showed that the proposed algorithm yielded accurate image reconstructions for different object field distributions designed in the experiment and could distinguish the shape and position information of the damage. This further verifies the feasibility of applying electromagnetic tomography technology to the nondestructive testing of hydrogen storage tanks.

For different application scenarios, the weights of conductivity and permeability need to be redetermined using SSIM to obtain the smaller error. Future research work will focus on detecting smaller defects and more forms of damage.

ACKNOWLEDGMENT

This research was funded by National Natural Science Foundation of China under Grant 62071328.

REFERENCES

1. Durbin, D. J. and C. Malardier-Jugroot, "Review of hydrogen storage techniques for on board vehicle applications," *International Journal of Hydrogen Energy*, Vol. 38, 14595–14617, 2013.
2. Hong, J.-H., M.-G. Han, and S.-H. Chang, "Safety evaluation of 70 MPa-capacity type III hydrogen pressure vessel considering material degradation of composites due to temperature rise," *Composite Structures*, Vol. 113, 127–133, 2014.

3. Liao, B. B., D. L. Wang, M. Hamdi, J. Y. Zheng, P. Jiang, C. H. Gu, and W. R. Hong, "Acoustic emission-based damage characterization of 70 MPa type IV hydrogen composite pressure vessels during hydraulic tests," *International Journal of Hydrogen Energy*, Vol. 44, 22494–22506, 2019.
4. Zhang, F., P. Zhao, M. Niu, et al., "The survey of key technologies in hydrogen energy storage," *International Journal of Hydrogen Energy*, Vol. 41, 1–18, 2016.
5. Ren, M.-F., X.-Zhang, C. Huang, et al., "An integrated macro/micro-scale approach for in situ evaluation of matrix cracking in the polymer matrix of cryogenic composite tanks," *Composite Structures*, Vol. 216, 201–212, 2019.
6. Meng, J., Y. Wang, H. Yang, et al., "Mechanical properties and internal microdefects evolution of carbon fiber reinforced polymer composites: Cryogenic temperature and thermocycling effects," *Composites Science and Technology*, Vol. 191, Nos. 1–2, 108083, 2020.
7. Wang, D., B. Liao, C. Hao, A. Wen, J. Zheng, P. Jiang, C. Gu, P. Xu, and Q. Huang, "Acoustic emission characteristics of used 70 MPa type IV hydrogen storage tanks during hydrostatic burst tests," *International Journal of Hydrogen Energy*, Vol. 46, 12605–12614, 2021.
8. Zhou, W., J. Wang, Z.-B. Pan, et al., "Review on optimization design, failure analysis and non-destructive testing of composite hydrogen storage vessel," *International Journal of Hydrogen Energy*, Vol. 47, 38862–38883, 2022.
9. Murray, B. R., S. B. Leen, C. O. A. Semprimoschnig, and C. M. O. Bradaigh, "Helium permeability of polymer materials as liners for composite overwrapped pressure vessels," *J. Appl. Polym. Sci.*, Vol. 133, No. 29, 43675, 2016.
10. Yang, B., Y. Xiang, F.-Z. Xuan, C. Hu, B. Xiao, S. Zhou, and C. Luo, "Damage localization in hydrogen storage vessel by guided waves based on a real-time monitoring system," *International Journal of Hydrogen Energy*, Vol. 44, 22740–22751, 2019.
11. Li, L. and F. Shao, "A threshold sensitivity method for image reconstruction of electromagnetic tomography," *International Congress on Image and Signal Processing*, Vol. 5, 2317–2321, 2010.
12. Wang, J. and X. Wang, "Application of particle filtering algorithm in image reconstruction of EMT," *Measurement Science and Technology*, Vol. 26, 2015.
13. Altin Karataş, M. and H. Gökkaya, "A review on machinability of carbon fiber reinforced polymer (CFRP) and glass fiber reinforced polymer (GFRP) composite materials," *Defence Technology*, Vol. 14, 318–326, 2018.
14. Ye, J., M. Mao, H. Wang, and W. Yang, "Image reconstruction for ECT based on extended sensitivity matrix," *IEEE Sensors Journal*, Vol. 16, 2466–2476, 2016.
15. Zhang, S., Y. Xu, and F. Dong, "Difference sensitivity matrix constructed for ultrasound modulated electrical resistance tomography," *Measurement Science and Technology*, Vol. 29, 104005 2018.
16. Zhang, L. and W. Yin, "Image reconstruction method along electrical field centre lines using a modified mixed normalization model for electrical capacitance tomography," *Flow Measurement and Instrumentation*, Vol. 62, 37–43, 2018.
17. Tang, K., H. Hu, L. Li, and X. Wang, "Composite sensitivity matrix for reducing the influence of medium electrification on electrical capacitance tomography," *IEEE Transactions on Instrumentation and Measurement*, Vol. 69, 1159–1169, 2020.
18. Gonzalez-Nakazawa, A., W. Yang, and K. Hennessey, "An analytical approach for modelling electro-magnetic tomography sensor," *Sensor Review*, Vol. 28, 212–221, 2008.
19. Liu, X., Z. Liu, and Y. Yue, "Simulation research of impact of number of coils in EMT sensors on reconstructed images quality," *Sensing & Imaging An International Journal*, Vol. 20, 1–13, 2019.
20. Liu, Z., W. Li, F. Xue, J. Xiafang, B. Bu, and Z. Yi, "Electromagnetic tomography rail defect inspection," *IEEE Transactions on Magnetics*, Vol. 51, 1–7, 2015.
21. Rodriguez, S., Y. Wang, R. Akid, R. Leiva, and W. Yin, "Design of an FPGA-based eddy current instrument for the detection of corrosion pits," *IEEE International Instrumentation and Measurement Technology Conference*, 705–710, 2015.
22. Yin, W. and A. J. Peyton, "Sensitivity formulation including velocity effects for electromagnetic induction systems," *IEEE Transactions on Magnetics*, Vol. 46, 1172–1176, 2010.

23. Wang, Q., H. Zhang, X. Li, X. Duan, J. Wang, R. Zhang, H. Zhang, Y. Ma, H. Wang, and J. Jia, "Error-constraint deep learning scheme for Electrical Impedance Tomography (EIT)," *IEEE Transactions on Instrumentation and Measurement*, Vol. 71, 1–11, 2022.
24. Yang, W. Q., D. M. Spink, T. A. York, and H. McCann, "An image-reconstruction algorithm based on Landweber's iteration method for electrical-capacitance tomography," *Measurement Science and Technology*, Vol. 10, 1065–1069, 1999.
25. Liu, Z., G. Yang, N. He, and X. Tan, "Landweber iterative algorithm based on regularization in electromagnetic tomography for multiphase flow measurement," *Flow Measurement and Instrumentation*, Vol. 27, 53–58, 2012.
26. Wang, T., D. Wu, W. Chen, and J. Yang, "Detection of delamination defects inside carbon fiber reinforced plastic laminates by measuring eddy-current loss," *Composite Structures*, Vol. 268, 114012, 2021.